Chapter 10

Geometric and Electronic Properties of Porphyrin and its Derivatives

Metin Aydin and Daniel L. Akins

Additional information is available at the end of the chapter

http://dx.doi.org/10.5772/64583

Abstract

In this chapter, we discuss protonation and substitution effects on the absorption spectra of porphyrin molecules based on density functional theory (DFT) and time-dependent DFT calculations. The results of the calculations are compared with experimental data. The calculations show that protonation of core nitrogen atoms of porphyrin and *meso*-substituted porphyrins produces a substantial shift in Soret and Q-absorption bands, relative to their positions in corresponding nonprotonated and nonsubstituted chromophores. A relaxed potential energy surface (RPES) scan has been utilized to calculate ground and excited state potential energy surface (PES) curves as functions of the rotation of one of the *meso*-substituted sulfonatophenyl groups about dihedral angles θ (corresponding to C_α—C_m—C_φ—C) ranging from 40 to 130°, using 10° increments. The ground state RPES curve indicates that when the molecule transitions from the lowest ground state to a local state, the calculated highest potential energy barrier at the dihedral angle of 90° is only 177 cm^{-1}. This finding suggests that the *meso*-sulfonatophenyl substitution groups are able to rotate around C_m—C_φ bond at room temperature because the thermal energy (k_BT) at 298 K is 207.2 cm^{-1}. Furthermore, the calculations show that the geometric structure of the porphyrin is strongly dependent on protonation and the nature of the *meso*-substituted functional groups.

Keywords: porphyrins, protonation, absorption, PES, DFT calculation

1. Introduction: overview of molecular spectroscopy and quantum calculations

Spectroscopy is the branch of science dealing with the interaction of electromagnetic and other forms of radiated energy with matter. The earliest prospect of making spectroscopic

measurements came with the observation that visible light can be dispersed by an optical prism, and the concomitant recognition that matter could be intimately investigated through its response to optical radiative energy as a function of frequency, defining what is referred to as optical spectroscopy. As it turns out, optical spectroscopy is a useful approach for both qualitative and quantitative studies of physical and chemical processes involving matter in most of its states by measurement of absorption, emission, or scattering of electromagnetic radiation; moreover, optical spectroscopic measurements can be very sensitive, nondestructive, and typically require only small amounts of material for analysis.

Absorption spectra are usually acquired for analytes dissolved in nonabsorbing solvents. And, ideally the absorbance of a dissolved analyte depends linearly on concentration, thereby resulting in an absorption spectrum providing quantitative measurement of the analyte's concentration in solution, arrived at by applying the Beer-Lambert Law. In particular, since absorption spectra of molecules depend on their energy level structure, absorption spectra are not only useful for identifying isolated molecules, but also can be used to probe intermolecular interactions (e.g., effects of aggregation) that affect energy level structure.

It is to be noted that molecules that are excited to higher energy than the lowest excited state above the ground electronic state can relax to lower excited levels by a range of intrinsic processes. Included among such deactivation processes are emission of radiation, more popularly referred to as luminescence, as well as processes that are nonradiative in nature, where lower energy states can be directly populated without the emission of photons. Luminescence from such intermediate states can be defined as fluorescence or phosphorescence, where fluorescence is a process by which electronically excited molecules return to a lower electronic state of the same spin multiplicity (which is often the electronic ground state) by emitting a photon; phosphorescence, on the other hand, is the corresponding transition between states with different spin multiplicities. While fluorescence is a spin-allowed process and generally occurs rapidly, phosphorescence is spin forbidden and is typically a slower relaxation process.

Paths by which nonradiative relaxation can occur include, but are not limited to, such phenomena as collisional energy transfer, electron or proton transfer processes, change of molecular conformation, photochemistry, formation of excited state complexes (e.g., excimers or exciplexes), as well as the classic processes of internal conversion (IC) (e.g., vibrational relaxation) and intersystem crossing (ISC) (e.g., singlet-triplet conversion).

It is to be noted that transient intermediates are likely to form during IC and ISC radiationless processes, and detection of such species, if at all possible, often necessitates the use of highly sensitive ultrafast optical (or other) techniques.

The aforementioned phenomena are depicted more fully in **Figure 1** that shows a combined Perrin-Jablonski diagram illustrating the different processes involved in the interaction of a molecule with photons in the spectral region between 300 and 1500 nm. Photophysical processes for an isolated molecule would occur via transitions between the different internal energy states shown in **Figure 1**.

http://dx.doi.org/10.5772/64583

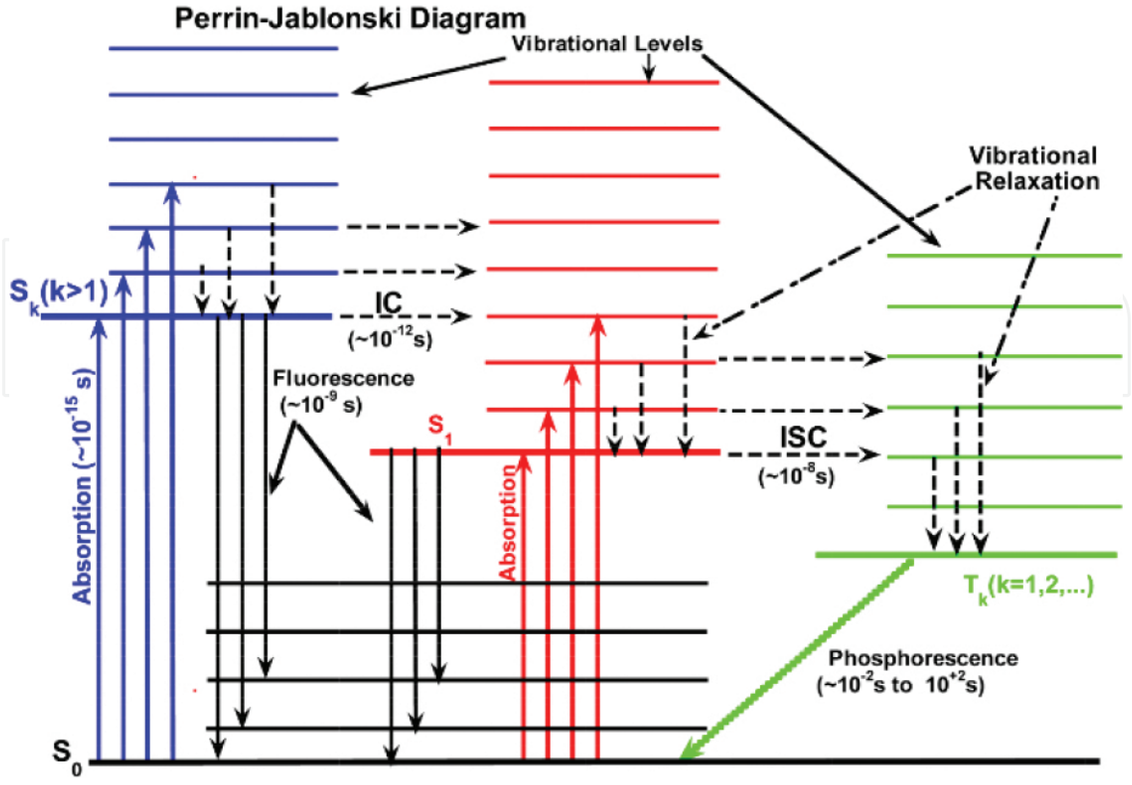

Figure 1. A general Perrin-Jablonski diagram, where S and T stand for singlet and triplet electronic states, respectively. IC and ISC represent "internal conversion" and "intersystem crossing," respectively.

Using **Figure 1** for discussion, in the gaseous or solution phase at room temperature a molecular system is generally in its ground state (S_0). The transition from the ground state to an upper vibroelectronic state by absorption of a photon would take place within ca. 10^{-15} s, which is much faster than the emission of the photon from an excited electronic state ($S_{k>1}$) to its ground state (ca. 10^{-8} s). As suggested earlier, all of the excited molecules might not directly return to their ground state by emission of radiation ($S_{k>0} \rightarrow S_0 + h\nu$), but some may return by internal conversion (IC). For example, when a molecule is excited to an upper vibroelectronic state ($S_k > 1$), it could undergo relaxation to the first excited singlet level S_1 (in 10^{-12} s) by way of vibrational coupling between these states before undergoing additional vibrational relaxation and returning to the lowest singlet electronic energy level (as per Kasha's Rule). As illustrated in **Figure 1**, another possible pathway is that a molecule in the first excited singlet level S_1 may undergo a transition to a triplet state by ISC, which can relax to the lowest triplet state (T_1) via vibrational relaxation and IC processes. The molecule can then return to its ground state through phosphorescence. There is also the possibility of a transition from T_1 to S_1 followed by the transition to S_0 by emitting a photon. This latter path is not shown in **Figure 1**.

During the past two decades, there has been very intense theoretical research on the physical and chemical properties of molecular structures. Computational chemistry is a powerful tool for investigation of molecules, surfaces, and interfaces at the electronic structure level. Various molecular properties directly comparable with experiment such as structural parameters, thermodynamic data, and vibrational spectra can be obtained by solving quantum mechanical

equations. When the result of a theoretical prediction is consistent with an experimental measurement, one can more confidently interpret the experimental result. Computational studies are not only carried out in order to provide an understanding of experimental data, such as the position and source of spectroscopic peaks, but also can be used to predict the existence of unobserved molecules, intermediates, or to explore reaction mechanisms that are not readily studied experimentally.

The particular computational method chosen depends critically on the desired accuracy (qualitative vs. quantitative) sought, the size of the system, and available computational capacities. At a qualitative level, especially for large systems, molecules can be treated by classical mechanics using a class of methods called molecular mechanics. The structure of a protein containing hundreds of atoms might be calculated this way. Somewhat more quantitatively accurate are the semiempirical methods. These methods (such as PM3) use experimentally measured parameters that approximate parts of a quantum mechanical system. These latter methods can be fast, and give good results if the molecule of interest is very similar to those used to determine the parameters. However, many molecules of interest (i.e., transition metal complexes) do not have sufficiently good parameter sets to be accurately calculated using such methods. *Ab initio* methods, however, do not assume experimental parameters, but instead attempt to calculate the molecular wave functions directly using a variety of approximation techniques. These methods, such as Hartree-Fock (HF) and MP2, can be very accurate for some observable phenomena, but can also be computationally expensive. HF with a mid-level basis set will often be used as a good starting point for more accurate calculations, or as a relatively fast way of getting qualitative data.

The fourth type of computational methods are the density functional theory (DFT) methods. With a few exceptions, DFT is the most cost-effective method to achieve a given level of quantitative accuracy. It incorporates electron correlation and is computationally less expense.

In addition to choosing a method, one must also choose a basis set. A basis set is a set of functions that substitute for the "real" atomic orbitals (AOs) of a system and should approximate the real wave functions well enough to give chemically meaningful and close approximations to the correct values of measurable quantities being considered (e.g., geometry and energy). Using more complex basis sets improves results at the cost of increased computer time to make a calculation (i.e., increased computational expense). Basis sets, in order to allow electron-electron correlation to be taken into account, must incorporate polarization terms to allow distortions in orbital shapes; they must also incorporate diffuse functions (especially necessary when you have a molecule with weakly bound electrons) (as in the case of some anions and for some transition states); and they must account for relativistic effects (for heavier atoms).

In this chapter, we will discuss protonation and *meso*-substitution effects on geometric and electronic structures of the porphyrin macrocycle based on quantum chemical methods. This chapter is also a sister publication for an accompanying article in another chapter of the present book entitled "Infrared and Raman Spectroscopic Characterization of Porphyrin and its Derivatives." Details about the calculations that we have made are provided in Section 4.

http://dx.doi.org/10.5772/64583

2. Porphyrin macrocycle

Porphyrin and its derivatives have received extensive attention from both experimentalists and theoreticians since they have been found to have many important potential applications in a broad variety of high technology and biomedical fields. Indeed, in recent years analyses of geometric and spectroscopic properties of molecular systems incorporating porphyrins have produced a substantial body of information that has greatly expanded our knowledge of high efficiency utilization of solar energy [1–5] and the use of such synthetic molecular analogs as active agents in molecular electronic devices [6, 7]. Also, a great deal of interest has been shown for the use of porphyrin-like molecular systems as therapeutic drugs and photosensitizers in photodynamic therapy of cancer [8] and their possible use in the treatment of nonmalignant conditions such as psoriasis, treatment of blocked arteries, and for the treatment of pathological and bacterial viruses [9] and HIV [10]. The biological importance of porphyrins essentially derives from their physicochemical properties that basically determine their photophysical behavior. Additionally, aggregation and axial ligation lead to significant changes in absorption spectra as well as quantum yield, fluorescence lifetime, and triplet state lifetime [11–13]. More detailed information about porphyrins can be obtained in the *Handbook of Porphyrin Science* [14, 15].

Of particular note is the observation that optical properties of porphyrin can be altered by the protonation or metallation of nitrogen atoms in its core structure, with electronic changes as a result of structural alterations such as flattening and distortion from planarity of the macrocycle, interactions between porphyrins (aggregation), redox reactions, and solvent effects. A few porphyrins have been found to form aggregates; a requirement of being zwitterionic character upon protonation of macrocycle core nitrogen atoms. It has also been suggested that aggregation is facilitated by interaction with proteins [16, 17] and surfactants [18].

Indeed, aggregation of the anionic porphyrin *meso*-tetrakis(*p*-sulfonatophenyl)porphyrin (TSPP) has been discussed extensively [9, 19–21]. The electronic absorption spectrum of monomeric TSPP at neutral pH exhibits multiple electronic transition bands with an intense peak maximum at about 410 nm and several weak transitions in the region of 500 to 700 nm in aqueous solutions. The intense transition at 410 nm is known as Soret or B-band, and the weaker bands are termed Q-bands. In very acidic medium, the TSPP becomes protonated, and one finds that highly ordered molecular aggregates are formed. While the protonated TSPP (i.e., H_4TSPP) shows a strong absorbance peak at around 430 nm (Soret band) along with the weak bands in the Q-bands region, the aggregated-H_4TSPP spectrum displays a Soret band at about 490 nm [21] and difference Q-type bands at longer wavelengths.

The developments in computing facilities and the sophisticated computation programs, with increasingly efficient algorithms, especially the fundamental improvements in the treatment of electron correlation based on density-functional theory (DFT) [22], have combined to allow quantum chemical methods to routinely handle molecular systems containing hundreds of atoms. As a result, DFT has become one of the most important techniques used by theoreticians

to provide deep insight into spectroscopic and structural properties, even for complex molecular systems, especially those of large sizes such as the porphyrinoids [23–28].

In this chapter, we discuss the effect of *meso*-substitution groups and protonation of the N atoms at the core (of parent-porphine or porphyrin macrocycle) of its geometric and electronic structures. The density functional theory (DFT) and time-dependent DFT (TD-DFT) have been employed to calculate the geometric structures and electronic transition energies of porphyrin and derivatives in water used as solvent. The compounds studied here are unsubstituted porphyrin (free-base porphin, FBP), *meso*-tetraphenylporphyrin (TPP), *meso*-tetrakis(*p*-sulfonatophenyl)porphyrin (TSPP), protonated-FBP (H_4FBP), deuterated-H_4FBP (D_4FBP), protonated-TPP (H_4TPP or dicationic TPP), deuterated-H_4TPP (D_4TPP), protonated-TSPP (H_4TSPP or dianionic-TSPP), deuterated-H_4TSPP (D_4TSPP),dicationic TSPP (H_8TSPP), and deuterated-H_8TSPP (D_8TSPP). The possible internal conversion (IC) and intersystem crossing (ISC) processes for the porphyrin and derivatives are also discussed based on the results of the TD-DFT calculations. Furthermore, the relaxed potential energy surface scans were employed to study the minimum potential energy pathways for the ground and excited states of the TSPP molecule as a function of rotation C_m—C_φ bond (or dihedral angle (C_α—C_m—C_φ—C(ph)). We would like to point out that the calculated and experimental data are taken from our prior work [29].

3. Structures of porphyrin and its derivatives

DFT theory at the B3LYP/6-311G(d,p) level was performed to predict the geometric parameters of the ground state of the parent porphyrin and its derivatives in water used as a solvent. The

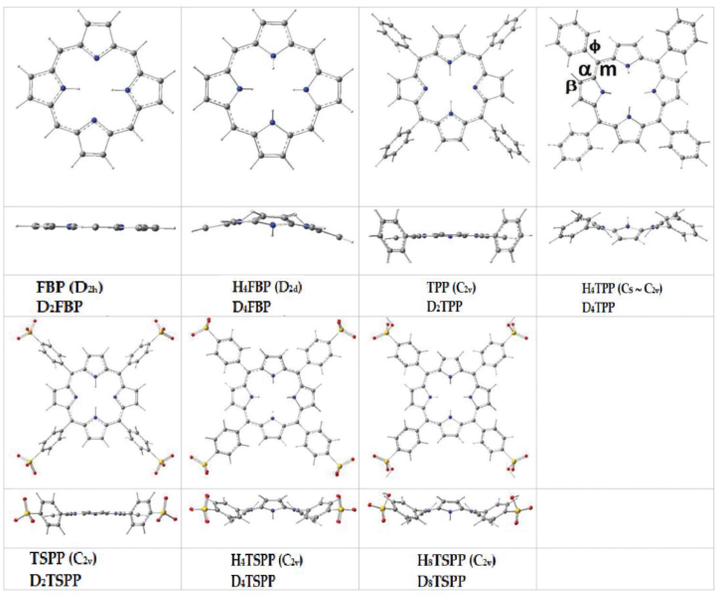

Figure 2. Optimized geometric structures of unsubstituted porphyrin (FBP), *meso*-tetraphenylporphyrin (TPP), anionic *meso*-tetrakis(*p*-sulfonatophenyl)porphyrin (TSPP), and their protonated derivatives (H_4FBP, H_4TPP, H_4TSPP, and H_8TSPP) in water at the B3LYP/6-311G(d,p) level of DFT.

optimized ground state geometry of these compounds is provided in **Figure 2**. The selected bond angles and dihedral angles are given in **Table 1**. Results of the calculations show that while the *meso* substitution of porphyrin with tetraphenyl or tetrasulfonatophenyl brings about slight out-of-plane distortion from the planar structure of the macrocycle within 3–5° for both TPP and TSPP, the protonation of the porphyrin core gives rise to a substantial distortion from planarity ranging from 10 to 20° for H_4FBP, H_4TPP, H_4TSPP, and H_8TSPP, principally due to repulsive interactions between the H atoms bonded to core N atoms. Moreover, with reference to the average plane of the macrocycle (**Figure 2** and **Table 1**), the peripheral phenyl and sulfonatophenyl substituents are tilted by an angle of about 72° for the nonprotonated structures TPP and TSPP, and about 48° for protonated H_4TPP, H_4TSPP, and H_8TSPP. Rotation of the *meso* substituents is attributed to repulsive interactions between H atoms on C_β and C in phenyl, as well electron correlation effect.

	FBP	**TPP**	**TSPP**	**H_4FBP**	**H_4TPP**	**H_4TSPP**	**H_8TSPP**
$D(C_\beta, C_\alpha, C_m, C_\varphi)$	N.A	3.6	4.0	N.A	19.4	19.6	19.0
$D(C_\beta, C_\alpha, C_m, C_{\alpha'})$	180.0	−176.5	−176.4	−169.5	−166.6	−160.5	−161.6
$D(C_\alpha, C_m, C_{\alpha'}, N)$	0.0	2.3	2.4	10.3	20.6	20.7	20.0
$D(C_\alpha, C_m, C_\varphi, C)$	N.A.	72.1	71.0	N.A	47.8	47.2	49.6
$D(C_\alpha, C_m, C_{\alpha'}, C_{\beta'})$	180.0	−177.2	−176.9	−169.5	−160.6	−160.5	−160.8
$D(C_m, C_{\alpha'}, C_{\beta'}, C_{\beta''})$	180.0	179.8	179.7	−178.8	−176.4	−174.4	−176.9
$D(C_{\alpha'}, C_{\beta'}, C_{\beta''}, C_{\alpha''})$	0.0	0.0	0.0	0.0	0.0	0.0	0.0
$D(C_{\beta'}, C_{\beta''}, C_{\alpha''}, C_{m'})$	180.0	−179.8	−179.7	178.8	176.4	176.4	176.9
$D(C_{\beta''}, C_{\alpha''}, C_{m'}, C_{\varphi'})$	N.A	−2.6	−2.6	N.A	−19.4	−19.4	−18.9
$D(C_{\alpha''}, C_{m'}, C_{\varphi'}, C)$	N.A	−72.1	−70.9	N.A	−47.8	−47.5	−49.9
$D(C_{\alpha'}, N, C_{\alpha''}, C_{\beta''})$	0.0	0.4	0.4	2.2	4.2	4.2	4.1
$A(C_\beta, C_\alpha, C_m)$	127.9	123.0	123.1	127.7	128.0	128.0	128.0
$A(C_\alpha, C_m, C_\varphi)$	N.A	118.2	118.2	N.A	118.3	118.3	118.2
$A(C_\varphi, C_m, C_{\alpha'})$	N.A	116.6	116.5	N.A	118.3	118.4	118.4
$A(C_\alpha, C_m, C_{\alpha'})$	127.0	125.2	125.3	127.4	123.4	123.4	123.9
$A(C_m, C_{\alpha'}, C_{\beta'})$	123.4	126.9	126.9	127.7	128.0	128.0	127.9
$A(N, C_\alpha, C_m)$	125.6	126.3	126.2	125.5	125.4	125.3	125.2
$A(C_m, C_{\alpha'}, N)$	125.7	126.6	126.6	125.5	125.4	125.3	125.3

Table 1. Comparison of selected dihedral angles (*D*) and bond angles (*A*) of the parent porphyrin and its derivatives: unsubstituted porphyrin (FBP), *meso*-tetraphenylporphyrin (TPP), and anionic *meso*-tetrakis(*p*-sulfonatophenyl) porphyrin (TSPP) with their protonated structures (H_4FBP, H_4TPP, H_4TSPP and H_8TSPP), calculated in water as solvent at the B3LYP/6-311G(d,p) level of DFT.

It is ascertained that the calculated bond lengths are consistent with X-ray data within ca. ± 0.01 Å. Hence, one can conclude that protonation of the porphyrin core, in addition to causing deviation from planarity of the macrocycle, also simply has an effect on the tilt angles of the phenyl and *p*-sulfonatophenyl substituent groups.

In Section 3.1, protonation and *meso* substitution of the porphyrin macrocycle is found to not only affect the geometric structure, but also, due to the change in molecular symmetry, lead to significant changes in electronic band positions as well as the number of bands.

3.1. Calculated electronic spectra of porphyrin and its derivatives

Porphyrin and its derivatives find use in a myriad of important natural and biomimetic processes, with the major focus in the latter case on processes such as conversion of solar energy into chemical energy, photodynamic therapy, and as active agents in optical sensors. The excited states of porphyrins play fundamental roles in essentially all processes involving porphyrin and its derivatives.

In this section, we discuss the *meso* substitution and protonation effects on the electronic energy levels of the porphyrin macrocycle. Up to 24 singlet and 24 triplet energy levels of porphyrins have been calculated in water used as solvent at the TD-B3LYP/6-31G(d,p) level; singlet-singlet absorption spectra have been calculated for these specific compounds and are provided in **Figure 3**.

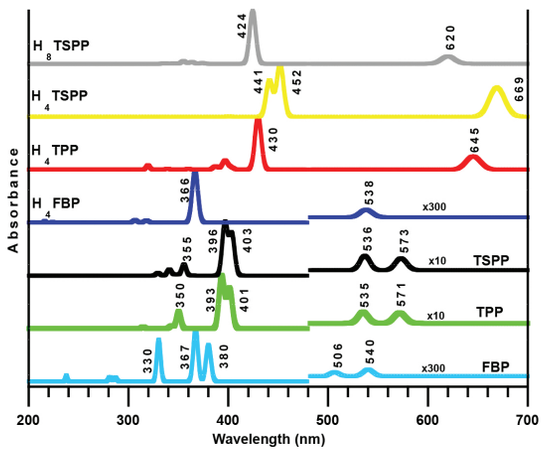

Figure 3. Comparison of calculated dipole-allowed electronic transitions of the parent porphyrin (FBP), *meso*-tetraphenylporphyrin (TPP), dianionic *meso*-tetrakis(*p*-sulfonatophenyl)porphyrin (TSPP), protonated-FBP (H_4FBP), protonated-TPP (H_4TPP), protonated TSPP (H_4TSPP), and dicationic-TSPP (H_8TSPP). The calculations were carried out in water used as a solvent at the TD-B3LYP/6-31G(d,p) level of TD-DFT.

The calculations mainly produce a strong electronic absorption band in the 360–450 nm range and a few weak or very weak electronic transitions below as well as above the strong bands (**Figure 3**). The strongest band is known as the Soret band (also referred to as the B-band), and weaker bands at longer wavelength, in the range 500–750 nm, are known as Q-bands that are usually quite weak. The results of calculations indicate that (1) the electronic bands in the parent porphyrin (FBP, neutral) are slightly blue-shifted in diprotonated-FBP (H_4FBP, dicationic) structure; (2) the bands in neutral TPP molecule (*meso*-phenyl substituted porphyrin) become significantly red-shifted in the dicationic or diprotonated-TPP (H_4TPP)—this observation indicates that the cationic macrocycle is stabilized by *meso*-substituted phenyl rings; (3) in the case of the *meso*-sulfonatophenyl substituted porphyrin ($TSPP^{-4}$, anionic), the electronic

bands in the TSPP are significantly red-shifted in both of the diprotonated porphyrin cores (H_4TSPP, dianionic) and in the protonation of the N atoms and sulfonato (SO_3^-) groups (H_8TSPP, dicationic)—but the red shift in band positions for the H_4TSPP is greater than that in H_8TSPP; and (4) bands in the nonprotonated and diprotonated porphyrin are significantly more red-shifted in its corresponding *meso*-phenyl/sulfonatophenyl structures. The electronic spectra of porphyrin and its derivatives studied here are discussed in more details in the next sections.

3.2. The electronic spectra of FBP and protonated-FBP (H_4FBP)

The electronic spectrum of the FBP molecule exhibited two weak electronic bands at wavelength longer than that of the Soret band (B): one of the bands corresponds to $S_0 \rightarrow S_1$ (B_{1u}, at 540 nm with oscillator strength $f = 0.0005$) resulting from H − 1 → L + 1 (40%) and H → L (59%), where H and L represent HOMO and LUMO, respectively; the second band corresponds to $S_0 \rightarrow S_2$ (B_{2u}, at 506 nm and $f = 0.0003$) resulting from H − 1 → L + 1 (47%) and H → L + 1 (53%).

There are also two strong electronic bands in the spectral range of the Soret band (B): one of the bands corresponds to $S_0 \rightarrow S_4$ (B_{2u}, at 367 nm and $f = 1.1911$) resulting from H − 1 → L (50%) and H → L + 1 (47%); the second band corresponds to $S_0 \rightarrow S_3$ (B_{1u}, at 380 nm and $f = 0.8144$) resulting from H − 1 → L (23%), H − 1 → L + 1 (49%), and H → L (30%).

A relatively strong band at 330 nm is also calculated as existing. One of these is due to the $S_0 \rightarrow S_7$ transition (B_{1u}, at 330 nm and $f = 0.6934$), H − 3 → L (76%), H − 1 → L + 1 (12%), and H → L (12%), while the second band at ca. 330 nm is assignable to the transition $S_0 \rightarrow S_8$ (B_{2u} and $f = 0.2479$) and transition H − 3 → L + 1 (93%). It is to be noted that a few weak bands in range of 330–200 nm are also calculated as existing (see **Table 2**).

The experimental absorption spectrum of FBP [30] exhibits absorption bands at about 372 and 340 nm in the Soret-band region. In the Q-band region, bands at about 512 and 626 nm are observed. The measured bands in the FBP spectrum are in good agreement with calculated values for the B-bands at 380, 367, and 340 nm, and for the Q-bands at 540 and 506 nm, but not for the weak band at 626 nm. In these band regions, the calculation did not produce any dipole-allowed or forbidden singlet-singlet transition. Therefore, the free-base porphin (FBP) sample may contain the free-base aza-porphin(s) (as aza substitution at the *meso* position). Moreover, the calculations indicated the internal-conversion (IC) process, from the Soret band ($S_{3/4}$ at 376 nm) to Q-bands (S_2 at 506 nm and S_1 at 540 nm), which is experimentally observed from the fluorescence spectra of sulfite reductase porphin methyl ester in chloroform, at the exciting light of 380 nm, showed two peaks at 597 and 640 nm [31]. We also calculated 24 triplet states ($S_0 \rightarrow T_n$) in the range of 249–822 nm for the FBP molecule. There are two triplet states: one $T_8(B_{3g})$ at 373 nm and the other $T_9(B_{2u})$ at 366 nm. The later one, $T_9(B_{2u})$ at 366 nm, closely overlaps with the strongly dipole-allowed electronic energy level $S_4(B_{2u})$ at 367 nm. This finding implies that there is not only the possibility of the internal-conversion (IC) process from the $S_{3/4}$ (B_{2u} at 376 nm) to S_2 (B_{2u} at 506 nm) and S_1 (B_{1u} at 540 nm), but also the possibility of the intersystem-crossing (ISC) process by way of the strong vibrational coupling between the singlet and triplet electronic states at $S_{3/4}$ at 376 nm and $T_{8/9}$ at 367 nm. The lowest triplet state

($S_0 \rightarrow T_1(B_{2u})$) was predicted at 822 nm resulting from H − 1 → L (21%) and H → L + 1 (79%) transitions.

FBP: $S_0 \rightarrow S_n$						**$S_0 \rightarrow T_n$**				
S_n	**(eV)**	**(nm)**	**f**	**Sym**	**Major contrib's**	**T_n**	**(eV)**	**(nm)**	**Sym**	**Major contrib's**
1	2.30	540	0.0005	B_{1U}	H − 1 → L + 1 (40%), H → L (59%)	1	1.51	822	B_{2U}	H − 1 → L (21%), H → L + 1 (79%)
2	2.45	506	0.0003	B_{2U}	H − 1 → L (47%), H → L + 1 (53%)	2	1.82	682	B_{1U}	H → L (94%)
3	3.26	380	0.8144	B_{1U}	H − 3 → L (22%), H − 1 → L + 1 (48%), H → L (29%)	3	2.04	608	B_{2U}	H − 1 → L (78%), H → L + 1 (22%)
4	3.38	367	1.1911	B_{2U}	H − 1 → L (50%), H → L + 1 (47%)	4	2.07	598	B_{1U}	H − 1 → L + 1 (94%)
5	3.44	360		B_{3G}	H − 2 → L (98%)	7	2.90	428	B_{3G}	H − 2 → L (88%)
6	3.66	339		A_G	H − 2 → L + 1 (99%)	8	2.96	419	B_{1U}	H − 3 → L (86%)
7	3.76	330	0.6934	B_{1U}	H − 3 → L (76%), H − 1 → L + 1 (12%), H → L (12%)	9	3.15	393	A_G	H − 2 → L + 1 (93%)
8	3.76	330	0.2479	B_{2U}	H − 3 → L + 1 (93%)	11	3.33	373	B_{3G}	H − 8 → L + 1 (16%), H → L + 2 (72%)
16	4.33	287	0.0914	B_{2U}	H − 5 → L + 1 (97%)	13	3.39	366	B_{2U}	H − 3 → L + 1 (96%)
18	4.41	281	0.1037	B_{1U}	H − 5 → L (99%)	15	3.61	343	A_G	H − 8 → L (26%), H − 1 → L + 2 (68%)
23	5.22	237	0.1338	B_{1U}	H − 2 → L + 2 (98%)	16	3.64	340	B_{3G}	H − 4 → L + 1 (79%)
H_4FBP: $S_0 \rightarrow S_n$						**$S_0 \rightarrow T_n$**				
S_n	**(eV)**	**(nm)**	**f**	**Sym**	**Major contrib's**	**T_n**	**(eV)**	**(nm)**	**Sym**	**Major contrib's**
1	2.31	538	0.0007	E	H − 1 → L + 1 (48%), H → L (52%)	1	1.63	763	E	H − 1 → L + 1 (30%), H → L (70%)
2	2.31	538	0.0007	E	H − 1 → L (48%), H → L + 1 (52%)	2	1.63	763	E	H − 1 → L (30%), H → L + 1 (70%)
3	3.39	366	1.4554	E	H − 1 → L + 1 (52%), H → L (48%)	3	1.96	632	E	H − 1 → L + 1 (69%), H → L (31%)
4	3.39	366	1.4554	E	H − 1 → L (52%), H → L + 1 (48%)	4	1.96	632	E	H − 1 → L (69%), H → L + 1 (31%)
7	3.90	318	0.0597	E	H − 5 → L + 1 (45%), H − 4 → L + 1 (53%)	7	3.23	384	B1	H − 3 → L + 1 (28%), H − 2 → L (28%), H → L + 2 (31%)
8	3.90	318	0.0597	E	H − 5 → L (45%), H − 4 → L (53%)	8	3.32	374	E	H − 3 → L + 1 (44%), H − 2 → L (44%)
11	4.05	306	0.0695	E	H − 5 → L + 1 (54%), H − 4 → L + 1 (45%)	9	3.37	367	E	H − 5 → L + 1 (42%), H − 4 → L + 1 (48%)
12	4.05	306	0.0695	E	H − 5 → L (54%), H − 4 → L (45%)	10	3.37	367	E	H − 5 → L (42%), H − 4 → L (48%)

Table 2. The selected values of the calculated singlet-singlet ($S_0 \rightarrow S_n$) and singlet-triplet ($S_0 \rightarrow T_n$) vertical electronic transitions with their oscillator strengths (f) for the FBP and protonated-FBP (H4FBP). The calculations were carried out in water used as a solvent at the TD-B3LYP/6-31G(d,p) level of TD-DFT. The percentages in parenthesis are the contributions from the different HOMO(H) → LUMO(L) transitions to a desired electronic transitions. The minor contributions are not given here.

http://dx.doi.org/10.5772/64583

The predicted electronic spectrum of protonated-FBP (H_4FBP) exhibits Q- and B-bands for $S_0 \rightarrow S_{1/2}$ (E at 538 nm with $f = 0.0007$) owing to H − 1 → L (48%) and H → L + 1 (52%) transitions; $S_0 \rightarrow S_{3/4}$ (E at 366 nm and $f = 1.4554$) owing to H − 1/ → L + 1 (53%) and H → L (49%) transitions. In addition, a few weaker transitions exist up to 300 nm (**Table 2**).

Comparing the electronic spectrum of FBP with that of H_4FBP: in FBP three strong bands were predicted at 380, 360, and 330 nm, see **Figure 3** and **Table 2**, whereas the H_4FBP spectrum exhibited only one strong band at 366 nm in the Soret-band region; in the Q-band region, H_4FBP has a doubly degenerate band at 538 nm, while FBP has two very weak transitions at 540 and 506 nm. This reduction in the number of bands is due to the higher symmetry for H_4FBP.

Also for FBP, the calculated electronic spectrum of diprotonated-FBP (i.e., H_4FBP) molecule indicates two IC processes from the $S_{3/4}$ (the strongest bands or B-band) at 366 nm (with the symmetry E) to the $S_{1/2}$ (at 538 nm with symmetry E), as well as the ISC process between the $S_{3/4}$ (at 366 nm) and $T_{7/8}$ (at 367 nm), see **Table 2**.

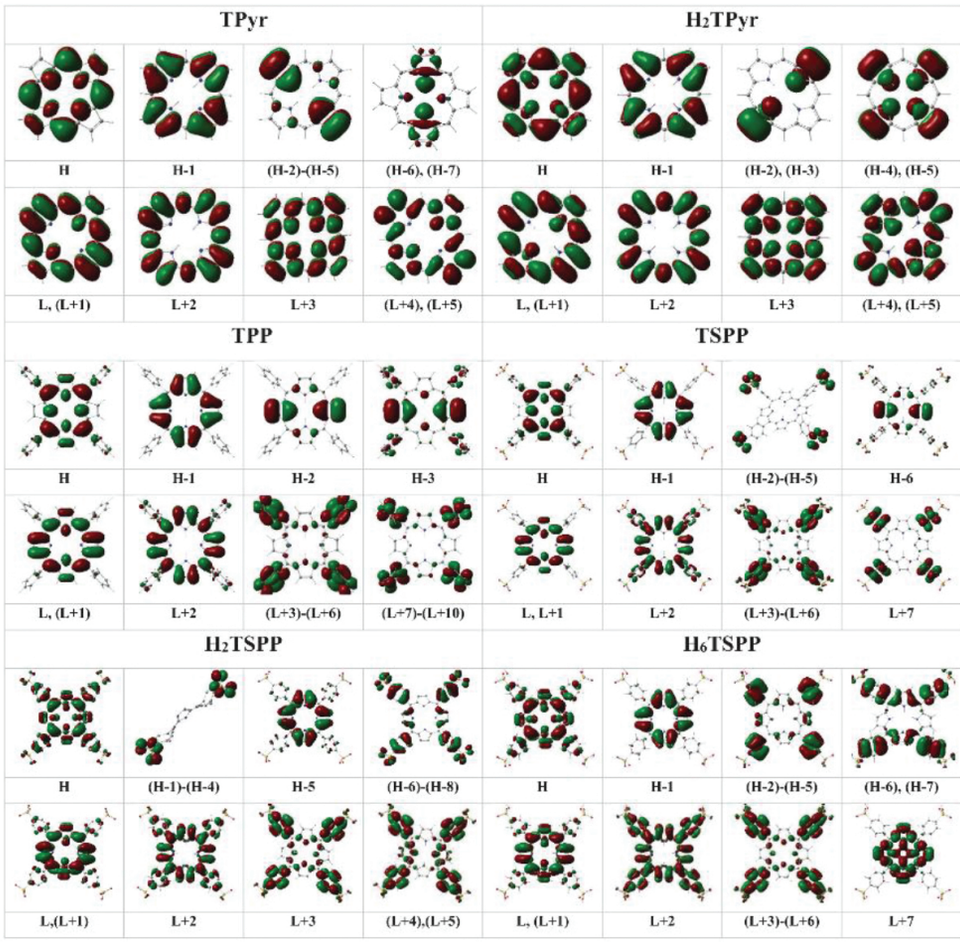

Figure 4. Plot of calculated electron densities in the desired HOMOs (H) and LUMOs (L) of parent porphyrin (FBP), *meso*-tetraphenylporphyrin (TPP), dianionic *meso*-tetrakis(*p*-sulfonatophenyl)porphyrin (TSPP), and protonated-FBP (H_4FBP), protonated-TPP (H_4TPP), protonated-TSPP (H_4TSPP), and dicationic-TSPP (H_8TSPP) molecules.

The electron density plots of the molecular orbitals (i.e., HOMOs (H) and LUMOs (L)), as seen in **Figure 4** and **Table 3**, show that the H − m and L + m (m = 0, 1, 2, …) are not just pure π and π^* molecular orbitals (MOs), in particular cases they also include nonbinding atomic orbitals (AOs).

FBP		**H_4FBP**	
H	$\pi(C_\beta{-}C_\beta/C_m{-}C_\alpha)$ + n(N)	H	$\pi(C_\beta{-}C_\beta/C_\alpha{-}C_m{-}C_\alpha)$ + n(N)
H − 1	$\pi(C_\beta{-}C_\alpha)$	H − 1	$\pi(C_\alpha{-}C_\beta)$
H − 2	$\pi(C_\alpha{-}N{-}C_\alpha/C_\beta{-}C_\beta)$	H − 2/H − 3	$\pi(C_\alpha{-}C_\beta)$ + n(N)
H − 3	$\pi(C_\alpha{-}N{-}C_\alpha/C_\beta{-}C_\beta)$ + n(minor, N/C_m)	H − 4/H − 5	$\pi(C_\beta{-}C_\beta)$ + n(N)
H − 4/H + 5	$\pi(C_\beta{-}C_\beta)$ + n(N)	H − 6/H − 7	$\pi(C_\beta{-}C_\alpha{-}C_m)$ + n(minor, N)
H − 6/H − 7	n(N) + σ(minor; $C_\beta{-}C_\alpha$)	H − 8	$\pi(C_\alpha{-}C_m{-}C_\alpha)$
L/L + 1	$\pi^*(C_\beta{-}C_\beta/C_\beta{-}C_\alpha/C_m{-}C_\alpha)$ + n(minor; N)	L/L + 1	$\pi(C_\beta{-}C_\alpha)$ + n(minor, N)
L + 2	$\pi^*(C_\beta{-}C_\alpha)$ + n(C_m)	L + 2	$\pi(C_\beta{-}C_\alpha)$ + n(C_m)
L + 3	$\pi^*(C_\beta{-}C_\beta/C_m{-}C_\alpha)$ + n(N/C_α)	L + 3	$\pi(C_\beta{-}C_\beta)$ + n(N/C_α/C_m)
L + 4/L + 5	$\pi^*(C_\beta{-}C_\beta/C_m{-}C_\alpha)$ + n(N/C_α/C_β)	L + 4	$\pi(C_\beta{-}C_\beta$ and $C_\alpha{-}C_m)$ + n(N/C_α/C_m)

Table 3. Bond type of the highest occupied molecular orbitals (H - m) and the lowest unoccupied molecular orbitals (L + m), m = 0, 1, 2, …

3.3. The electronic spectra of TPP and H_4TPP

While the calculated spectrum of the TPP molecule displayed two weak peaks at 571 ($S_0 \rightarrow S_1$, f = 0.00337) and 535 nm ($S_0 \rightarrow S_2$, f = 0.0359) in the region of the Q-absorption bands, the spectrum of diprotonated-TPP (H_4TPP) exhibited only a double degenerate peak that is also red-shifted to 645 nm ($S_0 \rightarrow S_{1/2}$, f = 0.3040). In the region of Soret band, two strong peaks were predicted at 401 and 393 nm ($S_0 \rightarrow S_{3/4}$, f = 1.2834/1.6972) in the TPP absorption spectrum, and the H_4TPP spectrum exhibited a doubly degenerate band at 430 nm ($S_0 \rightarrow S_{3/4}$, f = 1.209). Both spectra show a few weak and very weak-allowed electronic transitions in the high energy region as seen in **Table 4** and **Figure 5**. The observed spectrum of the **TPP** in **DMF** (Dimethylformamide) exhibited a strong band at about 412 nm with a shoulder at around 400 nm in Soret-band region, and four weak bands at about 513, 548, 590, and 645 nm in Q-band region (**Figure 5**). However, as shown in **Figure 5**, the calculated electronic spectrum of the TPP does not indicate any dipole-allowed or forbidden singlet-singlet transition with wavelength longer than 571 nm, rather, a weak singlet-singlet transition was predicated at 645 nm for the diprotonated-TPP (H_4TPP) molecule. This observation suggests that the TPP sample may contain a small percentage of aza-substituted TPP (at the beta or *meso* position) that produces weaker absorption peaks at around 590 and 646 nm. Another possibility might be that a small percentage of the TPP molecules in the sample might be at their local minima (instead of their ground state) due to rotation of the phenyl substitution at the *meso* position of TPP, resulting in weaker bands at around 590 and 646 nm.

TPP/$S_0 \rightarrow S_n$						$S_0 \rightarrow T_n$				
S_n	(eV)	(nm)	F	Sym	Major contrib's	T_n	(eV)	(nm)	Sym	Major contrib's
1	2.17	571	0.0337	B2	H − 1 → L + 1 (32%), H → L (67%)	1	1.40	884	B1	H − 1 → L (16%), H → L + 1 (84%)
2	2.32	535	0.0359	B1	H − 1 → L (37%), H → L + 1 (63%)	2	1.66	745	B2	H → L (98%)
3	3.09	401	1.2834	B2	H − 3 → L (10%), H − 1 → L + 1 (62%), H → L (27%)	3	1.99	623	B1	H − 1 → L (84%), H → L + 1 (15%)
4	3.16	393	1.6972	B1	H − 1 → L (62%), H → L + 1 (37%)	4	2.06	602	B2	H − 1 → L + 1 (97%)
6	3.54	350	0.5462	B2	H − 3 → L (87%)	5	2.84	436	A2	H − 2 → L (88%)
8	3.62	343	0.0909	B1	H − 3 → L + 1 (98%)	6	2.90	428	B2	H − 3 → L (82%)
19	3.95	314	0.0267	B1	H − 10 → L (39%), H − 8 → L + 1 (57%)	7	3.08	403	A1	H − 2 → L + 1 (91%)
20	3.95	314	0.0216	B2	H − 14 → L (15%), H − 11 → L (56%), H − 10 → L + 1 (14%), H − 8 → L (10%)	8	3.15	393	A2	H − 16 → L + 1 (10%), H → L + 2 (74%)
H_4 TPP/$S_0 \rightarrow S_n$						$S_0 \rightarrow T_n$				
S_n	(eV)	(nm)	F	Sym	Major contrib's	T_n	(eV)	(nm)	Sym	Major contrib's
1	1.92	645	0.304	A′	H − 1 → L + 1 (16%), H → L (84%)	1	1.22	1020	A″	H → L + 1 (98%)
2	1.92	645	0.3039	A″	H − 1 → L (16%), H → L + 1 (84%)	2	1.22	1020	A′	H → L (98%)
3	2.89	430	1.2029	A′	H − 1 → L + 1 (74%), H → L (14%)	3	2.02	615	A″	H − 1 → L (95%)
4	2.89	430	1.2026	A″	H − 1 → L (74%), H → L + 1 (14%)	4	2.02	615	A′	H − 1 → L + 1 (95%)
10	3.13	396	0.2053	A″	H − 5 → L (89%)	5	2.67	464	A″	H − 3 → L (13%), H − 2 → L + 1 (13%), H → L + 2 (56%)
11	3.13	396	0.2056	A′	H − 5 → L + 1 (89%)	6	2.76	449	A′	H − 7 → L + 1 (16%), H − 6 → L (16%), H − 3 → L + 1 (29%), H − 2 → L (29%)
15	3.20	387	0.078	A″	H − 8 → L (80%)	7	2.88	431	A′	H − 3 → L + 1 (46%), H − 2 → L (46%)
16	3.20	387	0.0778	A′	H − 8 → L + 1 (80%)	8	2.88	430	A″	H − 3 → L (46%), H − 2 → L + 1 (46%)
21	3.45	360	0.0351	A′	H − 10 → L (12%), H − 9 → L (80%)	9	2.93	424	A′	H − 5 → L + 1 (82%)
22	3.66	339	0.039	A″	H − 10 → L + 1 (13%), H − 9 → L + 1 (80%)	10	2.93	424	A″	H − 5 → L (82%)

Table 4. Selected values of the calculated singlet-singlet ($S_0 \rightarrow S_n$) and singlet-triplet ($S_0 \rightarrow T_n$) vertical electronic transitions with their oscillator strength (f) for the TPP and H4TPP. The percentages in parenthesis are the contributions from the various HOMO (H) to LUMO (L) transitions to a desired electronic transitions. The minor contributions are not given here. The calculations were carried out in water as solvent at the TD-B3LYP/6-31G(d,p) level of TD-DFT.

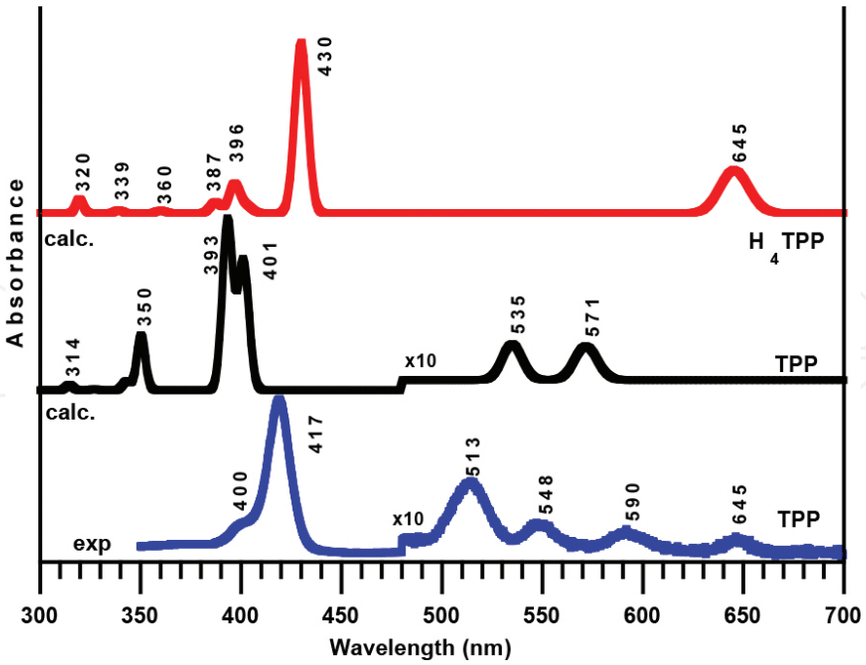

Figure 5. Calculated and measured absorption spectra of TPP and calculated absorption spectrum of protonated-TPP (H_4TPP).

TPP			
H	$\pi(C_\alpha{-}C_m{-}C_\alpha/C_\beta{-}C_\beta) + n(N \text{ and } C_\varphi)$	L/L + 1	$\pi^*(C_\beta{-}C_\beta/C_\beta{-}C_\alpha/C_m{-}C_\alpha) + n^*(N(H))$
H − 1	$\pi(C_\alpha{-}C_\beta)$	L + 2	$\pi^*(C_\alpha{-}C_m) + n^*(C_\varphi)$
H − m m = 2, 3	$\pi(C_\beta{-}C_\beta)/\ \pi(N{-}C_\alpha{-}C_m)$	L + m m = 3–6	π^*(C—C in phenyl)

Table 5. Bond type of the highest occupied molecular orbitals (H − m) and the lowest unoccupied molecular orbitals (L + m), m = 0, 1, 2, ….

Furthermore, Jiang *et al*. [32] measured absorption and EPR spectra of some porphyrins (TPP and derivatives) and metalloporphyrins compounds, and the measured absorption spectrum of TPP produced an intense electronic transition centered about 417 nm (B-band) and several Q-bands with weak intensities around 514, 550, 590, and 646 nm. The authors have also stated that both steric hindrance and electronic effects of the functional groups influenced the UV-vis absorption of the TPP, with the Soret bands of the *para*-substituted *meso*-tetraphenylporphine derivatives somewhat red-shifted (3–5 nm). This experimental observation is consistent with the result of our calculations (**Figure 5** and **Tables 2–5**).

Additionally, the results of the calculations for TPP (in solution/water) indicate the possibility of an IC process from S_6 (B_2 at 350 nm)/S_4 (B_1 at 393 nm)/S_3 (B_2 at 401 nm) to S_2 (B_1 at 535 nm) and S_1 (B_2 at 571 nm), which are verified by experimental measurements of the fluorescence spectrum of the TPP in different environments. Moreover, based on theoretical predictions,

there are strong surface crossings between the singlet-triplet excited states of the TPP: S_4 (B_1 at 393 nm) and T_8 (A_2 at 393 nm), and S_3 (B_2 at 401 nm) and T_7 (A_1 at 403 nm), which may cause an ISC process in the excited state.

The results of the calculated electronic energy states of diprotonated-TPP molecule (H_4TPP) indicate the existence of an IC process from the $S_{3/4}$ (A′ and A′′′ at 430 nm) to $S_{1/2}$ (A′ and A″ at 645 nm), in addition to possibility of an ISC process between the $S_{3/4}$ (A′ and A″ at 430 nm) and $T_{7/8}$ (at 431 and 430 nm, with symmetry A′ and A″, respectively).

3.4. Calculated electronic spectra of TSPP, H_4TSPP, and H_8TSPP

In the Q-band region, while the calculations indicate the presence of two weak transitions at 573 nm ($S_0 \rightarrow S_1$ with symmetry B_2 and $f = 0.0419$) and at 536 nm ($S_0 \rightarrow S_2$ with symmetry B_1, $f = 0.0506$) in the TSPP spectrum, the calculated spectrum of H_4TSPP shows two doubly degenerate peaks at 669 nm ($S_0 \rightarrow S_{1/2}$ with symmetries B_2 and B_1 with $f = 0.4223/0.4138$) and at 528 nm ($S_0 \rightarrow S_{4/5}$ with symmetries A_1 and B_2 and $f = 0.0001/0.0005$), in addition to a band at 518 nm ($S_0 \rightarrow S_{10}$, B_2 symmetry and $f = 0.0001$). However, the spectrum of the dicationic-TSPP (H_8TSPP) indicates almost overlapping (or nearly degenerate) weak electronic transitions at 620 nm ($S_0 \rightarrow S_1$ with symmetries B_2, $f = 0.2467$) and at 619 nm ($S_0 \rightarrow S_2$ with symmetries B_1, $f = 0.2377$).

In the B-band (Soret band) region, while the calculated spectrum of the TSPP exhibited two strong bands at 403 nm ($S_0 \rightarrow S_3$ with B_2 symmetry and $f = 1.4382$) and at 396 nm ($S_0 \rightarrow S_4$ with symmetry B_1 and $f = 1.8378$), the H_4TSPP spectrum contains two strong bands at 452/451 nm ($S_0 \rightarrow S_{12/13}$, B_1 and B_2 symmetries, $f = 0.7601/0.7369$) and a medium intense band at 441 nm ($S_0 \rightarrow S_{16}$, B_2 symmetry and $f = 0.5315$). The calculated spectrum of the dicationic-TSPP (H_8TSPP) exhibits a double degenerate strong transitions at 424 nm ($S_0 \rightarrow S_{3/4}$, with B_1 and B_2 symmetries and $f = 1.7153/1.7145$, respectively). Additionally, many weak electronic transitions are predicted at longer wavelengths than these strong Soret bands (see **Table 6**). The predicted B-bands and Q-bands for the molecules studied here are compatible with the experimental data [21, 33].

Akins *et al.* [21] and Zhang *et al*. [33] have reported the UV-vis spectra of the free-base TSPP and the H_4TSPP (dianionic-TSPP). While the measured absorption spectrum of the TSPP displayed an intense band (S-band, also known as B-band) at ~412 nm, and several very weak broad bands (known as Q-bands) at about 517 (± 2), 555 (± 3), 581 (± 3), and 640 (± 3) nm, the H_4TSPP spectrum exhibited the B-band at 432 nm and very weak broad Q-bands at 589 (± 5) and 645 nm. However, in the Q-band region, the calculations produced only two very weak dipole-allowed electronic transitions at 536 and 573 nm for the TSPP and only one doubly degenerated band at 669 nm for the H_4TSPP. The calculated absorption spectra suggest that the two of four absorption bands in TSPP and one of two bands for the H_4TSPP, in the Q-region, must be due to vibrational progression such as from the lowest vibrational level in the electronic ground state to higher vibrational level in electronically excited state, $S_0(\nu'' = 0)$ to $S_Q(\nu' \geq 1)$.

TSPP:$S_0 \rightarrow S_n$						$S_0 \rightarrow T_n$				
S_n	(eV)	(nm)	f	Sym	Major contrib's	T_n	(eV)	(nm)	Sym	Major contrib's
5	2.16	573	0.0419	B2	H − 1 → L + 1 (32%), H → L (67%)	1	1.40	884	B1	H − 1 → L (16%), H → L + 1 (86%)
6	2.31	536	0.0506	B1	H − 1 → L (36%), H → L + 1 (64%)	2	1.67	744	B2	H → L (97%)
10	3.07	403	1.4382	B2	H − 1 → L + 1 (62%), H → L (28%)	3	1.99	624	B1	H − 1 → L (84%), H → L + 1 (15%)
11	3.13	396	1.8378	B1	H − 1 → L (62%), H → L + 1 (36%)	4	2.05	604	B2	H − 1 → L + 1 (97%)
36	3.49	355	0.3924	B2	H − 10 → L (83%)	5	2.84	437	A2	H − 9 → L (49%), H − 7 → L (39%)
38	3.56	348	0.0392	B1	H − 10 → L + 1 (28%), H − 8 → L (69%)	6	2.89	429	B2	H − 11 → L (36%), H − 10 → L (48%)
47	3.64	341	0.2178	B2	H − 11 → L (83%)	7	3.07	404	A1	H − 9 → L + 1 (39%), H − 7 → L + 1 (51%)
48	3.77	329	0.0936	B1	H − 11 → L + 1 (82%), H − 10 → L + 1 (11%)	8	3.14	395	A2	H → L + 2 (70%)

H_4TSPP:$S_0 \rightarrow S_n$						$S_0 \rightarrow T_n$				
S_n	eV	(nm)	f	Sym.	Major contrib's	T_n	eV	(nm)	Sym	Major contrib's
1	1.85	669	**0.4223**	B2	H − 5 → L + 1 (13%), H → L (87%)	1	1.17	1056	B2	H → L (97%)
2	1.85	669	**0.4138**	B1	H − 5 → L (13%), H → L + 1 (87%)	2	2.01	618	B1	H − 5 → L (95%)
4	2.35	528	**0.0001**	A1	H − 3 → L + 1 (47%), H − 2 → L (53%)	3	2.34	530	A1	H − 3 → L + 1 (47%), H − 2 → L (52%)
5	2.35	528	**0.0005**	B2	H − 4 → L (53%), H − 1 → L + 1 (47%)	5	2.34	529	B1	H − 4 → L + 1 (47%), H − 1 → L (52%)
10	2.40	518	**0.0001**	B2	H − 4 → L (47%), H − 1 → L + 1 (53%)	9	2.39	518	A1	H − 3 → L + 1 (53%), H − 2 → L (47%)
12	2.74	452	**0.7601**	B1	H − 6 → L (79%), H − 5 → L (15%)	13	2.51	494	A2	H − 8 → L + 1 (34%), H − 7 → L (35%), H → L + 2 (23%)
13	2.75	451	**0.7369**	B2	H − 6 → L + 1 (83%), H − 5 → L + 1 (12%)	14	2.62	474	B1	H − 6 → L (90%)
16	2.81	441	**0.5315**	B2	H − 9 → L (17%), H − 6 → L + 1 (16%), H − 5 → L + 1 (57%)	17	2.65	467	A1	H − 8 → L (46%), H − 7 → L + 1 (46%)
18	2.81	441	**0.5073**	B1	H − 9 → L + 1 (16%), H − 6 → L (19%), H − 5 → L (54%)	18	2.69	462	A2	H − 8 → L + 1 (47%), H − 7 → L (47%)

19	2.97	417	**0.0013**	B1	H − 13 → L (14%), H − 10 → L + 1 (74%)	19	2.72	455	A2	H − 8 → L + 1 (13%), H − 7 → L (12%), H → L + 2 (63%)
22	3.10	400	**0.0081**	B2	H − 13 → L + 1 (12%), H − 10 → L (82%)	20	2.96	419	A2	H − 12 → L + 1 (43%), H − 11 → L (47%)

H_8TSPP:S_0 →S_n						**S_0→T_n**				
S_n	**eV**	**(nm)**	**f**	**Sym.**	**Major contrib's**	**T_n**	**(eV)**	**(nm)**	**Sym**	**Major contrib's**
1	2.00	620	0.2467	B2	H − 1 → L + 1 (23%), H → L (77%)	1	1.31	946	B2	H → L (96%)
2	2.00	619	0.2377	B1	H − 1 → L (23%), H → L + 1 (77%)	2	1.31	945	B1	H → L + 1 (96%)
3	2.92	424	1.7153	B1	H − 1 → L (74%), H → L + 1 (23%)	3	1.94	639	B1	H − 1 → L (94%)
4	2.92	424	1.7145	B2	H − 1 → L + 1 (75%), H → L (22%)	4	1.94	638	B2	H − 1 → L + 1 (94%)
7	3.32	374	0.0199	B2	H − 4 → L (92%)	5	2.74	452	A2	H → L + 2 (72%)
8	3.32	373	0.0240	B1	H − 4 → L + 1 (92%)	6	3.00	413	A1	H − 7 → L (26%), H − 6 → L + 1 (26%), H − 3 → L (13%), H − 2 → L + 1 (18%)
11	3.41	363	0.0560	B1	H − 5 → L (88%)	7	3.08	403	A2	H − 3 → L + 1 (37%), H − 2 → L (40%)
12	3.42	363	0.0614	B2	H − 5 → L + 1 (88%)	8	3.09	401	A1	H − 3 → L (36%), H − 2 → L + 1 (34%), H − 1 → L + 2 (14%)
15	3.50	355	0.0822	B1	H − 8 → L (94%)	9	3.16	393	B2	H − 5 → L + 1 (16%), H − 4 → L (66%)
16	3.50	355	0.0918	B2	H − 8 → L + 1 (94%)	10	3.16	393	B1	H − 5 → L (17%), H − 4 → L + 1 (65%)
20	3.59	346	0.0365	B2	H − 10 → L (10%), H − 9 → L (84%)	11	3.20	387	A2	H − 12 → L + 1 (11%), H − 11 → L (12%), H − 7 → L + 1 (29%), H − 6 → L (30%)
21	3.69	336	0.0363	B1	H − 10 → L + 1 12%), H − 9 → L + 1 (81%)	12	3.23	384	B1	H − 8 → L (66%)

Table 6. The selected values of the calculated singlet-singlet (**S_0→S_n**) and singlet-triplet (**S_0→T_n**) vertical electronic transitions with oscillator strength (f) for the TSPP and protonated-TSPP (H4TSPP). The calculations were carried out in water used as a solvent at TD-B3LYP/6-31G(d,p) level of the TD-DFT. The percentages in the parenthesis indicate the contributions from the different HOMO(H) → LUMO(L) transitions to a desired electronic transitions. The minor contributions are not given here.

Also, Akins and coworkers have measured fluorescence spectra of free-base TSPP (pH = 12), monomeric H_4TSPP (pH = 4.5), and aggregate H_4TSPP in highly acidic situation. The authors reported that the fluorescence spectrum of the TSPP at 412 nm (B-band region) excitation displayed a peak at 642 nm with a red degraded shoulder at 702 nm. The spectrum of H_4TSPP upon excitation at 432 nm in the B-band region exhibited similar structure, for example, a strong emission peak at 665 nm with relatively weak shoulder at about 716 nm [21]. Both fluorescence spectra of the TSPP and deprotonated-TSPP (H_4TSPP) indicated that when excited in the Soret- or B-band region, initially internal conversion (IC) occurs from the B-band to the Q-bands, followed by a fluorescence from the lowest excited state(s) in Q-band region to the ground state S_0 a sequence of: $S_0 + h\nu_0 \rightarrow S(\text{B-band}) \rightarrow S(\text{Q-band}) \rightarrow S_0 + h\nu$. These observations are consistent with our calculations. For instance, the predicted possible IC (internal-conversion) process may take place from the S_3 (at 403 nm) to S_1 (at 573 nm) and S_2 (at 536 nm) for the TSPP; and from the $S_{12/13}$ (at 452/451 nm)/S_{16} (at 441 nm) to S_{10} (at 518 nm)/$S_{4/5}$(at 528 nm)/$S_{1/2}$(at 669 nm) for the H_4TSPP (diprotonated- or dianionic-TSPP).

The calculations also indicate that there might be an ISC (intersystem crossing) process between the S_3 (at 403 nm)/S_4 (at 396 nm) and the T_7 (at 404 nm)/T_8 (at 395 nm), and between the S_1 (at 573 nm) and T_4 (at 604nm) for TSPP (where the energy difference between S_1 and T_4 states is about 0.11 eV or 896 cm^{-1}). For the H_4TSPP (or dianionic-TSPP), the ISC process may occur between the $S_{4/5}$ (at 528 nm) and $T_{3,4,5,6}$ (at 530 and 529 nm), and S_{10} (at 518 nm) and $T_{15,16,17,18}$ (at 518 nm), and between the S_1(669 nm) and T_3(618 nm) (where the energy difference between the S_1(669 nm) and T_3(618 nm) states is 0.15 eV or 1233 cm^{-1}) (**Figure 6**). The results of the calculations suggest that, depending on competition between the IC and ISC processes, there can be ISC through vibrational coupling or potential energy surface (PES) touching between singlet and triplet states.

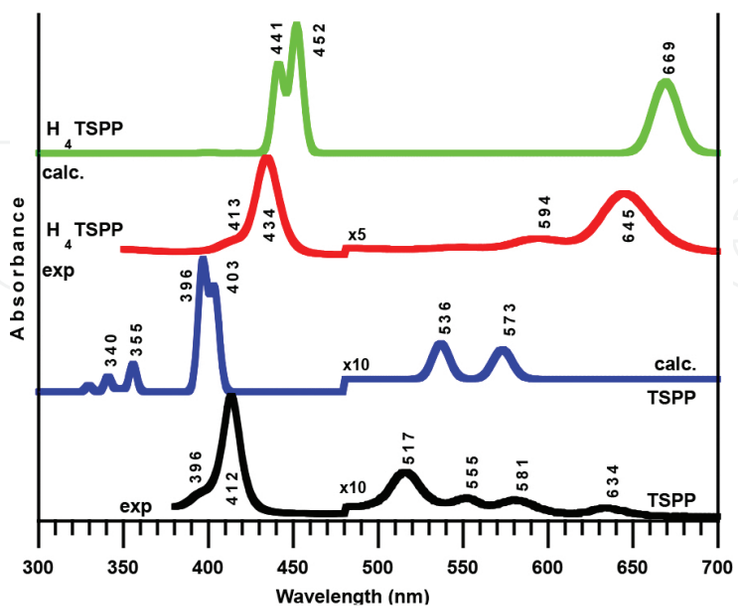

Figure 6. Calculated and measured absorption spectra of TSPP and protonated-TSPP (H_4TSPP).

Likewise, for the H_8TSPP (dicationic-TSPP molecule), the IC process may happen from the B-bands ($S_{3/4}$ at 424 nm) to the Q-bands ($S_{1/2}$ at 620/619 nm). Furthermore, the energy difference between the $S_{1/2}$ (at 424/424 nm) and $T_{3/4}$ (at 639/637 nm) is about 0.056 eV or 455 cm^{-1}, which may lead to a strong vibrational coupling in their excited vibroelectronic states. Owing to this small energy distance between singlet and triplet states of the H_8TSPP, there would likely occur ISC that may originate from B-bands ($S_{1/2}$) to triplet states ($T_{3/4}$).

TSPP		**H_4TSPP**		**H_8TSPP**	
H	$\pi(C_\alpha{-}C_m{-}C_\alpha/C_\beta{-}C_\beta)$ + n(N and C_φ/C(S))	H	$\pi(C_\alpha{-}C_m{-}C_\alpha/C_\beta{-}C_\beta$/C–C in phenyl) + n(N)	H	$\pi(C_\alpha{-}C_m{-}C_\alpha/C_\beta{-}C_\beta)$ + n(N and C_φ/C(S) in phenyl)
H − 1	$\pi(C_\alpha{-}C_\alpha)$	H − m m = 1–4	n(O)	H − 1	$\pi(C_\alpha{-}C_\beta)$
H − m m = 2–5	n(O)	H − 5	$\pi(C_\alpha{-}C_\beta)$	H − m m = 2–5	π(C–C–C in phenyl) + n(C_α and C_β, minor)
H − 6	$\pi(C_\beta{-}C_\beta$ and $C_\alpha{-}N{-}C_\alpha)$	H − m m = 6–8	π(C–C–C in phenyl) + minor n(O and C_β)	H − 6/H − 7	π(C(S)–C/C–C_φ in phenyl and $C_m{-}C_\alpha{-}C_\beta$)
L/L + 1	$\pi^*(C_\beta{-}C_\alpha/C_\beta{-}C_\beta$ and $C_\alpha{-}C_m)$ + n*(N(H))	L/L + 1	$\pi^*(C_\alpha{-}C_m/C_\beta{-}C_\beta)$ + n*(N)	L/L + 1	$\pi^*(C_\alpha{-}C_m/C_\beta{-}C_\beta)$ + n*(N);
L + 2	$\pi^*(C_\varphi{-}C_m/C_\alpha{-}C_m)$ + n*(C(S), minor)	L + 2	$\pi^*(C_\varphi{-}C_m/C_\beta{-}C_\alpha)$ and minor n*(C in phenyl)	L + 2	$\pi^*(C_\varphi{-}C_m/C_\beta{-}C_\beta$ and C–C/C–S in phenyl)
L + m m = 3–6	π*(C–C in phenyl)	L + m m = 3–5	π*(C–C in phenyl) + n*(C(S) and C_φ in phenyl)	L + m m = 3–6	π*(C–C/C–S in phenyl) and n*(C_φ)/n*(C_α and N, minor)

Table 7. Bond type of the highest occupied molecular orbitals (H − m) and the lowest unoccupied molecular orbitals (L + m), m = 0, 1, 2, …

Consequently, the results of calculated absorption spectra for the porphyrin molecules studied here (**Tables 2–7**) reveal several important points: (1) protonation of the N atoms at the porphyrin core and the *meso* substitutions of the parent porphyrin with the phenyl or sulfonatophenyl groups lead to substantial red-shifts in the spectral position of the Soret bands and Q-bands; (2) the IC process takes place from the B-band(s) to the Q-band(s) for the all porphyrin derivatives; (3) an ISC process might be possible through the surface touching and/or strong vibrational coupling, but would be dependent on the competition with IC processes and the rate constant of fluorescence; and (4) deuteration of the N atoms at the core of the macrocycle and O atoms do not produce significant change in their corresponding spectra.

3.5. Relaxed potential energy surface (RPES) scan of TSPP molecule

The relaxed potential energy surface (RPES) scan was performed to calculate the ground state PES of the TSPP molecule in water by rotating one of four dihedral angles θ ($C_\alpha{-}C_m{-}C_\varphi{-}C$)

from 40 to 130° in 10° increments. The calculated ground state curve, S_0(RPES), shows two minima at dihedral angles of ~66 and 110° (see **Figure 7(B)** and **(C)**). These two minima on the S_0(RPES) curve represent the lowest ground state with C_{2v} symmetry and an energetically stable local state with C_2 symmetry, respectively. The local minima at 110° is about 106 cm^{-1} (0.0132 eV) above the lowest ground state at 66° as seen in **Figure 7(C)**. When the molecule goes from the lowest ground state to this local state, the predicted highest potential energy barrier at the dihedral angle of 90° is only 177 cm^{-1} (0.0219 eV). This finding suggests that the *meso*-substituted sulfonatophenyl groups are able to rotate around C_m—C_φ bond at room temperature because the thermal energy (k_BT) at 298 K is 207.2 cm^{-1}. Consequently, since the computed potential energy barrier is small as much as 106 cm^{-1} at the dihedral angle of 90°, the self-assembling of the TSPP molecules in any environment might be very easily formed. It should be point out that the calculated ground state RPES was carried out only for the rotation of one of four *meso*-sulfonatophenyl groups within the TSPP molecule. If the RPES scans were performed for the rotations of all four *meso*-substitutional groups, there would be more than a few different local minima with dissimilar potential energy barriers on the ground state RPES. Thereby, a slight change in the potential energy barrier distribution of the *meso*-substituted porphyrin molecules, such as the TSPP, can be used as a scanning nanocalorimetric measurement (or for other electronic purposes) of very small variations in energy.

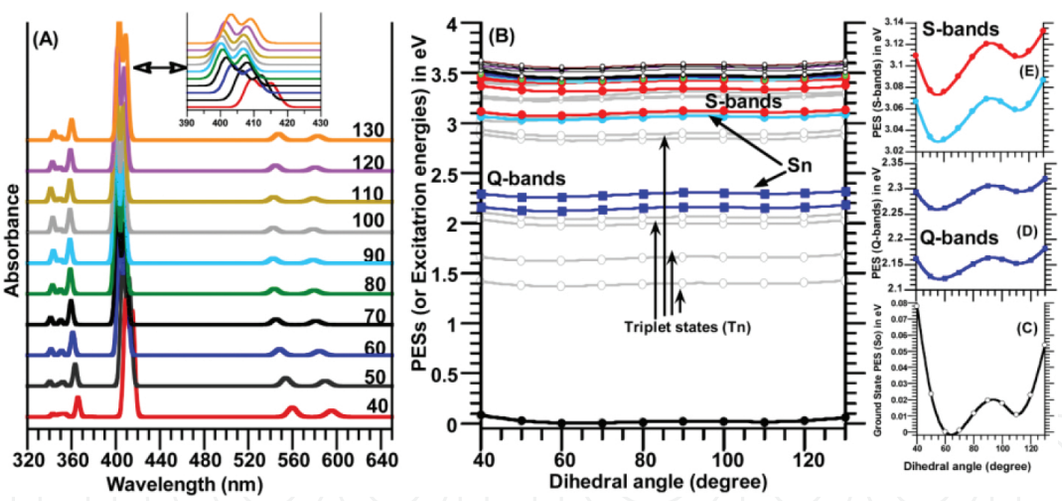

Figure 7. The calculated spectra of the TSPP as a function of the dihedral angle (C_α—C_m—C_φ—C(ph)) rotation varying from 40 to 130° with 10° increment: (A) plot of dipole-allowed singlet electronic transitions $S_0 \rightarrow S_n$, with n = 1–24; (B) the relaxed potential energy surfaces of the ground state (S_0) and upper singlet (S_n) and triplet (T_n) states, n = 1–24; (C)–(E) illustrate the RPES curves for the ground state S_0, Q-bands and Soret bands at a low scale for a better view. It is noteworthy that only one of the four *meso*-sulfonatophenyl groups is rotated about the C_m—C_φ bond and the uppercase letter S in (E) symbolizes the Soret band.

It is to be noted that the PES curves of the upper singlet (S_n) and triplet (T_n) energy states were calculated by the following Eqs. (1) and (2), respectively:

$$V_n(S_n, \theta) = E(\theta) - E_0 + E(S_0 \rightarrow S_n; \theta) \quad (1)$$

$$V_n(T_n, \theta) = E(\theta) - E_0 + E(S_0 \rightarrow T_n; \theta) \quad (2)$$

(1) In the aforementioned equations, E_0 and $E(\theta)$ symbolize the calculated global (total SCF) energies at the lowest ground state and the relaxed potential energy at the dihedral angle $\theta(C_\alpha{-}C_m{-}C_\varphi{-}C_1)$, respectively; $E(S_0 \rightarrow S_n/S_0 \rightarrow T_n; \theta)$ represents the vertical electronic transition energy from S_0 to excited electronic energy levels S_n/T_n at the dihedral angle θ. It is to be noted that **Figure 7(A)** displays the computed dipole-allowed electronic transitions at each rotated dihedral angle, $\theta(C_\alpha{-}C_m{-}C_\varphi{-}C_1)$, while **Figure 7(C)–(E)** shows the alteration in the calculated singlet and triplet electronic energy levels as a function of the $\theta(C_\alpha{-}C_m{-}C_\varphi{-}C_1)$. The PES curves of the excited states S_n and T_n are akin to the ground state RPES, S_0(RPES). Consequently, the results of the calculations indicated that the red-shift in spectral position of the Soret bands increases with increasing rotational dihedral angle in both right-handed and left-handed rotational directions around the equilibrium dihedral angle of ~66° in the ground state.

4. Calculation section

The calculations were carried out in water used as solvent at the B3LYP level of the density functional theory (DFT) [34, 35] with the 6-311G(d,p) basis set [36]. The solvent effects were considered by using the self-consistent reaction field (SCRF) calculations [37] with the conductor-like polarizable continuum model [38–40] and a dielectric constant of 78.39 for water; SCRF = (CPCM, solvent = water) as implemented within the Gaussian 09 software package [41]. All compounds studied here were optimized to minima on their ground state relaxed potential energy surfaces (RPESs) that were verified by revealing the absence of imaginary frequencies in calculated vibrational spectra. Time-dependent DFT (TD-DFT) was performed to calculate the first 24 singlet-singlet ($S_0 \rightarrow S_n$) and singlet-triplet ($S_0 \rightarrow T_n$; n = 1 to 24) vertical electronic transitions in water. Finally, to investigate the dependence of the potential energy of the ground state (S_0) and excited states (S_n and T_n) on the rotation of the $C_m{-}C_\varphi$ bond, we used the Gaussian keyword "Opt = ModRedundant." The calculated ground state (S_0) potential energies at each optimized structure were plotted as a function of the rotated dihedral angle θ in the region of 40–130° with 10° increment. The potential energy surfaces of the singlet and triplet excited states were conducted by calculating the singlet-singlet, $S_0 \rightarrow S_n$, and singlet-triplet, $S_0 \rightarrow T_n$, electronic transition energies for each optimized structure at the rotated dihedral angle θ, including the SCF energy correction to each calculated electronic transition energy, $\Delta ESCF = E(\theta) - E0$, where $E(0)$ and $E(\theta)$ represent the calculated global energies of the ground state and energetically most stable structure at the dihedral angle θ, respectively.

We would like to point out that the electron densities in HOMO and LUMO molecular orbitals, and electronic spectra of the molecules studied here were plotted using GaussSum software [42].

Acknowledgements

We would like to thank the following: the U.S. National Science Foundation (NSF) for support of research efforts under grant no. HRD-08-33180 and Ömer Andaç (of the Chemistry Department of Ondokuz Mayıs University) for kindly making available computing facilities and software setup. We also thank TUBITAK ULAKBIM, High Performance and Grid Computing Center (TR-Grid e-Infrastructure) for performing the calculations reported in this work.

Author details

Metin Aydin[1*] and Daniel L. Akins[2]

*Address all correspondence to: aydn123@netscape.net

1 Department of Chemistry, Faculty of Art and Sciences, Ondokuz Mayıs University, Samsun, Turkey

2 Department of Chemistry and Biochemistry, Center for Analysis of Structures and Interfaces (CASI), The City College of the City University of New York, New York, USA

References

[1] Dolphin, D. *The Porphyrins*; Dolphin, D., Ed.; Academic Press: New York, 1978; Volume 1–3.

[2] Shelnutt, J. A,; Alston, K.; Findsen, E. W.; Ondrias, M. R.; Rifkind, J. M. In *Polphyrins: Excited States and Dynamics*; Gouterman, M., Rentzepis, P. M., Straub, K. D., Eds.; ACS Symposium Series 321; American Chemical Society: Washington, DC, 1986; Chapter 16.

[3] Brunner, H.; Nishiyama, H.; Itoh, K. in *Catalytic Asymmetric Synthesis*; Ojima, I. (Ed.), VCH, New York, 1993, pp. 303–322.

[4] Lu, J., Li, H., Liu, S., Chang, Y-C., Wu, H-P., Cheng, Y., Diau, E. W-G., Wang, M. Novel porphyrin-preparation, characterization, and applications in solar energy conversion. *Phys.Chem.Chem.Phys*. 2016, 18, 6885.

[5] Bian, Y.; Zhang, Y.; Ou, Z.; Jiang, J. Chemistry of Sandwich Tetrapyrrole Rare Earth Complexes. Handbook of Porphyrin Science, World Scientific Publishing, Singapore, 2011, 14, 249–460.

[6] Holten, D.; Bocian, D.F. Probing electronic communication in covalently linked multiporphyrin arrays. A guide to the rational design of molecular photonic devices. *J.S. Acc. Chem. Res*. 2002, *35*, 57–69.

[7] Hopfield, J.J.; Onuchic, J.N.; Beratan, D.N. A molecular shift register based on electron transfer. *Science* 1988, *241*, 817–820.

[8] Bonnett, R. Photosensitizers of the porphyrin and phthalocyanine series for photodynamic theory. *Chem. Soc. Rev*. 1995, *24*, 19–33.

[9] Andrade, S.M.; Costa, S.M.B. Spectroscopic studies on the interaction of a water soluble porphyrin and two drug carrier proteins. *Biophys. J.* 2002, *82*, 1607–1619.

[10] Ben-Hur, E.; Horowitz, B. Advances in photochemical approaches for blood sterilization. *Photochem. Photobiol.* 1995, *62*, 383–388.

[11] Uhehara, K.; Hioki, Y.; Mimuro, M. The chlorophyll *a* aggregate absorbing near 685 nm is selectively formed in aqueous tetrahydrofuran. *Photochem. Photobiol.* 1993, *58*, 127–132.

[12] Tominaga, T.T.; Yushmanov, V.E.; Borissevitch, I.E.; Imasato, H.; Tabak, M. Aggregation phenomena in the complexes of iron tetraphenylporphine sulfonate with bovine serum albumin. *J. Inorg. Biochem*. 1997, 65, 235–244.

[13] Togashi, D.M.; Costa, S.M.B. Absorption, fluorescence and transient triplet-triplet absorption spectra of zinc tetramethylpyridylporphyrin in reverse micelles and microemulsions of aerosol OT-(AOT). *Phys. Chem. Chem. Phys*. 2000, *2*, 5437–5444.

[14] Ferreira, G. C.; Kadish, K. M.; Smith, K. M.; Guilard, R., Eds. In *The Handbook of Porphyrin Science*; World Scientific Publishers: Singapore, 2013, Vol. 27.

[15] Gillam, M. E.; Hunter, G. A.; Ferreira, G. C. The ultimate step of heme biosynthesis: orchestration between iron trafficking and porphyrin synthesis. In *Heme Biochemistry*; Ferreira, G.C., Ed., of *The Handbook of Porphyrin Science* series, Kadish, K. M.; Smith, K. M.; Guilard, R. series Eds., World Scientific Publishing Co., New Jersey, USA, 2013, Vol. 26, pp. 129–189.

[16] Borissevitch, I.E.; Tominaga, T.T.; Imasato, H.; Tabak M. Fluorescence and optical absorption study of interaction of two water soluble porphyrins with bovine serum albumin: the role of albumin and porphyrin aggregation. *J. Luminesc.* 1996, *69*, 65–76.

[17] Huang, C.Z.; Li, Y.F.; Li, K.A.; Tong, S.Y. Spectral characteristics of the aggregation of α, β, γ, δ-tetrakis(*p*-sulfophenyl)porphyrin in the presence of proteins. *Bull. Chem. Soc. Jpn.* 1998, *71*, 1791–1797.

[18] Maiti, N.C.; Ravikanth, M.; Mazumdar, S.; Periasamy N. Fluorescence dynamics of noncovalent linked porphyrin dimers and aggregates. *J. Phys. Chem.* 1995, *99*, 17192–17197.

[19] Ohno, O.; Kaizu, Y.; Kobayashi, H. J-aggregate formation of a water-soluble porphyrin in acidic aqueous media. *J. Chem. Phys.* 1993, *99*, 4128–4139.

[20] Akins, D.L.; Zhu, H.-R.; Guo, C. Absorption and Raman scattering by aggregated meso-tetrakis(p-sulfonatophenyl)porphine. *J. Phys. Chem.* 1994, *98*, 3612–3618.

[21] Akins, D.L.; Özçelik, S.; Zhu, H.R.; Guo, C. Fluorescence decay kinetics and structure of aggregated tetrakis(*p*-sulfonatophenyl)porphyrin. *J. Phys. Chem.* 1996, *100*, 14390–14396.

[22] Labanowski, J.K.; Andzelm, J.W. *Density Functional Theory Methods in Chemistry*; Springer-Verlag: New York, NY, USA, 1991.

[23] Aydin, M. DFT and Raman spectroscopy of porphyrin derivatives: tetraphenylporphine (TPP). *Vib. Spectrosc.* 2013, *68*, 141–152.

[24] Słota, R.; Broda, M.A.; Dyrda, G.; Ejsmont, K.; Mele, G. Structural and molecular characterization of meso-substituted zinc porphyrins: a DFT supported study. *Molecules* 2011, *16*, 9957–9971.

[25] Wang, C.; Yang, G.; Li, J.; Mele, G.; Słota, R.; Broda, M.A.; Duan, M.; Vasapollo, G.; Zhang, X.; Zhang, F.X. Novel meso-substituted porphyrins: synthesis, characterization and photocatalytic activity of their TiO2-based composites. *Dyes Pigments* 2009, *80*, 321–328.

[26] Zhang, Y.H.; Zhao, W.; Jiang, P.; Zhang, L.J.; Zhang, T.; Wang, J. Structural parameters and vibrational spectra of a series of zinc meso-phenylporphyrins: a DFT and experimental study. *Spectrochim. Acta A* 2010, *75*, 880–890.

[27] Yao, P.; Han, S.; Zhang, Y.; Zhang, X.; Jiang, J. Structures and spectroscopic properties of mesotetrasubstituted porphyrin complexes: Meso-Substitutional and central metallic effect study based on density functional theory calculations. *Vib. Spectrosc*. 2009, *50*, 169–177.

[28] De Oliveira, V.E.; Cimini Correa, C.; Pinheiro, C.B.; Diniz, R.; de Oliveira, L.F.C. Structural and spectroscopy studies of the zinc complex of p-hydroxyphenylporphyrin. *J. Mol. Struct*. 2011, *995*, 125–129.

[29] Aydin, M. Comparative study of the structural and vibroelectronic properties of porphyrin and its derivatives. *Molecules* 2014, *19*, 20988–21021.

[30] Edwards, L.; Dolphin, D. H.; Gouterman, M.; Adler, A. D. Porphyrins XVII. Vapor absorption spectra and redox reactions: Tetraphenylporphins and porphin. J Mol Spectrosc 1971, 38, 16.

[31] Murphy, M. J.; Siegel, L. M.; Kamin, H.; Rosenthal, D. Reduced nicotinamide adenine dinucleotide phosphate-sulfite reductase of enterobacteria. II. Identification of a new class of heme prosthetic group: an iron-tetrahydroporphyrin (isobacteriochlorin type) with eight carboxylic acid groups. J Biol Chem. 1973, 248(8), 2801–2814.

[32] Lan, M.; Zhao, H.; Yuan, H.; Jiang, C.; Zuo, S.; Jiang, Y. Absorption and EPR spectra of some porphyrins and metalloporphyrins. *Dyes Pigments* 2007, *74*, 357–362.

[33] Zhang, Y.H.; Chen, D.M.; He, T.; Liu, F.C. Raman and infrared spectral study of meso-sulfonatophenyl substituted porphyrins (TPPSn, n_/1, 2A, 2O, 3, 4). *Spectrochim. Acta Part A* 2003, *59*, 87–101.

[34] Becke, A.D. Density-functional thermochemistry. III. The role of exact exchange. *J. Chem. Phys*. 1993, *98*, 5648–5652.

[35] Lee, C.; Yang, W.; Parr, R.G. Development of the Colle-Salvetti correlation-energy formula into a functional of the electron density. *Phys. Rev. B* 1988, *37*, 785–789.

[36] Krishnan, R.; Binkley, J.S.; Seeger, R.; Pople, J.A. Self-consistent molecular orbital methods. XX. A basis set for correlated wave functions.. *J. Chem. Phys.* 1980, *72*, 650–654.

[37] Tomasi, J.; Mennucci, B.; Cammi, R. Quantum mechanical continuum solvation Models. *Chem. Rev*. 2005, *105*, 2999–3093.

[38] Barone, V.; Cossi, M. Quantum calculation of molecular energies and energy gradients in solution by a conductor solvent model. *J. Phys. Chem. A* 1998, *102*, 1995–2001.

[39] Miertus, S.; Scrocco, E.; Tomasi, J. Electrostatic interaction of a solute with a continuum. A direct utilization of ab initio molecular potentials for the prevision of solvent effects. *Chem. Phys*. 1981, *55*, 117–129.

[40] Cossi, M.; Rega, N.; Scalmani, G.; Barone, V. Energies, structures, and electronic properties of molecules in solution with the C-PCM solvation model. *J. Comput. Chem*. 2003, *24*, 669–681.

[41] Frisch, M.J.; Trucks, G.W.; Schlegel, H.B.; Scuseria, G.E.; Robb, M.A.; Cheeseman, J.R.; Scalmani, G.; Barone, V.; Mennucci, B.; Petersson, G.A.; *et al*. *Gaussian 09, Revision A. 02*. Gaussian. Inc.: Wallingford, CT, 2009, 200.

[42] O'Boyle, N. M.; Tenderholt, A. L.; Langner, K. M. A library for package-independent computational chemistry algorithms. *J. Comp. Chem*. 2008, *29*, 839–845.

IntechOpen